In Situ Formation of Metal Oxide Nanocrystals Embedded in Laser-Induced Graphene

Ruquan Ye,[†,#] Zhiwei Peng,[†,#] Tuo Wang,[†] Yunong Xu,[⊥] Jibo Zhang,[†] Yilun Li,[†] Lizanne G. Nilewski,[†] Jian Lin,[§,∥] and James M. Tour*[,†,‡,§]

[†]Department of Chemistry, [⊥]Department of Computational and Applied Mathematics, [‡]Smalley Institute for Nanoscale Science and Technology, and [§]Department of Materials Science and NanoEngineering, Rice University, 6100 Main Street, Houston, Texas 77005, United States and [∥]Department of Mechanical & Aerospace Engineering, University of Missouri, Columbia, Missouri 65211, United States. [#]R. Ye and Z. Peng contributed equally to this work.

ABSTRACT Hybrid materials incorporating the advantages of graphene and nanoparticles have been widely studied. Here we develop an improved cost-effective approach for preparation of porous graphene embedded with various types of nanoparticles. Direct laser scribing on metal-complex-containing polyimide film leads to *in situ* formation of nanoparticles embedded in porous graphene. These materials are highly active in electrochemical oxygen reduction reactions, converting O_2 into OH^-, with a low metal loading of less than 1 at. %. In addition, the nanoparticles can vary from metal oxide to metal dichalcogenides through lateral doping, making the composite active in other electrocatalytic reactions such as hydrogen evolution.

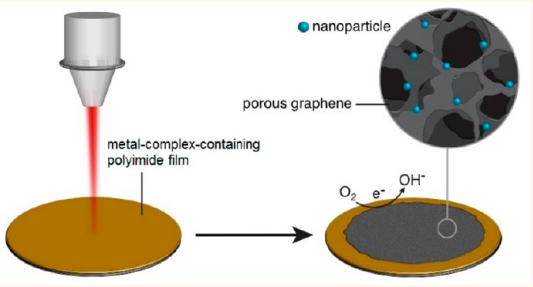

KEYWORDS: laser-induced graphene · porous graphene · electrochemical oxygen reduction reaction · hydrogen evolution

Graphene is a unique material that has been widely investigated and found to have broad applications in fields such as energy storage,[1,2] electronics,[3,4] and electrocatalysis.[5,6] Exploiting the advanced properties of graphene, such as high electrical conductivity,[7,8] excellent chemical and mechanical stability,[9,10] and large specific surface area,[11] hybrid materials made by combining graphene with nanoparticles[12−17] have led to products with much improved physical and chemical characteristics. These hybrid materials may possess superior performance when compared to either graphene or nanoparticles by themselves. This implies that there is a synergistic interaction between the graphene and nanoparticles.[12,18] The production of the graphene−nanoparticle hybrids using industrial processes such as roll-to-roll manufacturing continues to be a technical challenge. One of the challenges is the lengthy process, including graphene oxide synthesis, nanoparticle deposition, and graphene oxide reduction.[19−21] Such an approach may require high reaction temperatures, a large consumption of unrecoverable solvents and acids, and/or considerable time periods, in addition to the stepwise electrode preparation.

We demonstrate here an improved method for direct preparation of metal oxide nanoparticle/graphene hybrid materials by laser induction. It has been shown that exposure of polyimide (PI) film to laser radiation leads to formation of porous 3D graphene.[2,22,23] In this work, by scribing a CO_2 infrared laser on a metal-complex-containing polyimide (MC-PI) film, crystalline nanoparticles that are embedded in porous graphene are formed. The method demonstrated here is complementary to the conventional preparation process, as it starts with polyimide films that contain metal, avoids the traditional GO synthesis step that constitutes the major proportion of the cost of the product, and is applicable to roll-to-roll manufacturing processes. Hybrids prepared from mechanical mixing of graphene and metal oxide can be seemingly straightforward, but the performance is usually inferior compared to those prepared from wet-chemistry integration.[24−26]

* Address correspondence to tour@rice.edu.

Received for review July 6, 2015 and accepted August 18, 2015.

Published online August 18, 2015
10.1021/acsnano.5b04138

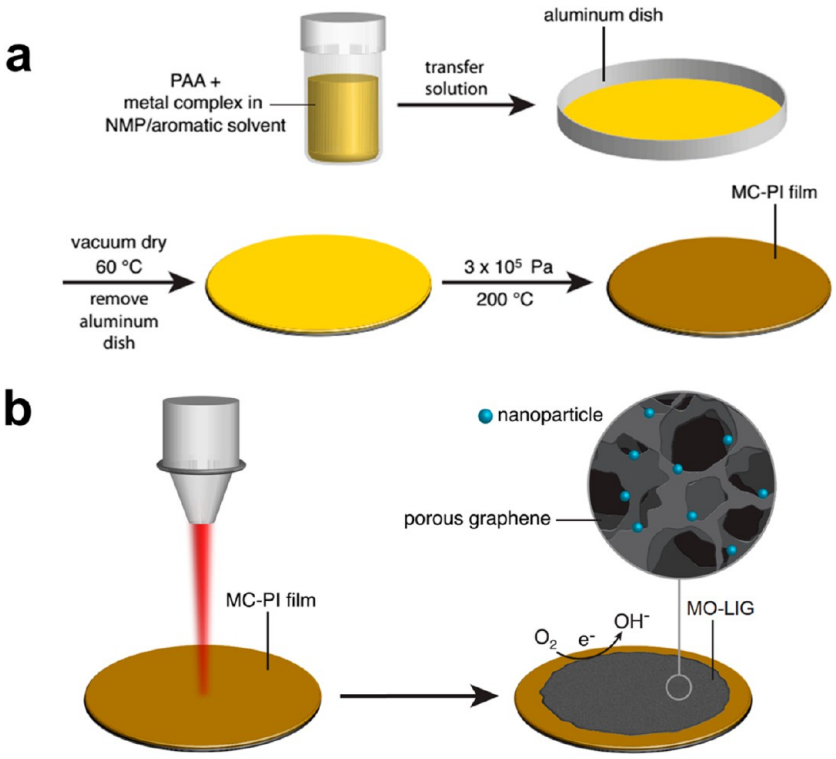

Scheme 1. Schematic illustration of formation of MO-LIG from MC-PI film. (a) Preparation of MC-PI film from metal-complex-containing PAA solution. A MC-PAA film forms from evaporation of solvent in the metal-complex-containing PAA solution in an aluminum dish. After dehydration of PAA by heating at 200 °C under pressure, a MC-PI forms. (b) Formation of MO-LIG by laser induction on MC-PI film. The MC-PI film was subjected to a 10.6 μm CO_2 laser. The area induced by the laser turns into a porous structure (black region), and the area without laser-induction remains unchanged.

Here we show that these printable films, after annealing under argon, are effective electrocatalysts in converting O_2 to OH^-, making them possible substitutes for platinum in oxygen reduction reaction (ORR) fuel cell applications. Moreover, the nanoparticle composition is tunable by altering the metal complex or the lateral doping, producing materials with potential applications in various other electrocatalytic applications such as the hydrogen evolution reaction (HER) or oxygen evolution reaction (OER).

RESULTS AND DISCUSSION

Preparation of MC-PI Film. As shown in Scheme 1a, the metal complex cobalt(III) acetylacetonate, iron(III) acetylacetonate, or molybdenyl(VI) acetylacetonate in *N*-methyl-2-pyrrolidone (NMP) was mixed with a 12.8 wt % solution of poly(pyromellitic dianhydride-*co*-4,4′-oxidianiline amic acid) (PAA) in NMP/aromatic solvent (80:20). A brownish film was formed after removal of the solvent under vacuum and further heat and pressure treatment to condense the PAA to form a PI film (Methods).

Preparation of Metal Oxide Nanocrystals Embedded in Laser-Induced Graphene. As depicted in Scheme 1b, after irradiation of the MC-PI film by a CO_2 infrared laser under ambient conditions, the compact MC-PI film was transformed into 3D porous laser-induced graphene (LIG) with embedded metal oxide (MO) nanocrystals (MO-LIG). A typical MO-LIG film is shown in Figure S1a. Depending on the precursor metal complex used, we formed metal oxide nanocrystals of Co_3O_4, MoO_2, and Fe_3O_4. The corresponding MO-LIGs are termed 5X-LIG, with X = Co, Mo, or Fe, where "5" signifies the wt % of the metal complex (MC) precursor in the precursor solution (Scheme 1a, PAA + solvent + 5 wt % of MC). After the laser scribing process, MO-LIGs were annealed at 750 °C for 30 min under argon (Methods). The corresponding MO-LIGs after annealing (MO-LIG-A) are termed 5X-LIG-A, where "A" stands for annealed.

Structure Characterization. The morphology of MO-LIG and MO-LIG-A was investigated by scanning electron microscopy (SEM) and transmission electron microscopy (TEM). As shown in the SEM images (Figure 1a–f), a porous structure of 3D graphene forms after the laser scribing process, which is similar to our previous findings.[2,22,23] The Brunauer–Emmett–Teller (BET) surface areas of the MO-LIG are summarized in Table S1, with surface areas of ~180 $m^2\ g^{-1}$. These values are similar to our previous results from homemade polymer[23] and smaller than the ones from commercial Kapton (~330 m^2/g).[2,22] Figure 1d–f show the TEM images of 5Co-LIG, 5Mo-LIG, and 5Fe-LIG; the corresponding average diameters of the nanocrystals are 9.8 ± 3.3, 5.3 ± 1.3, and 14 ± 5.5 nm (Figure S1b–d). The corresponding SEM images of MO-LIG-A after annealing are shown in Figure S2a–c. The annealing process led

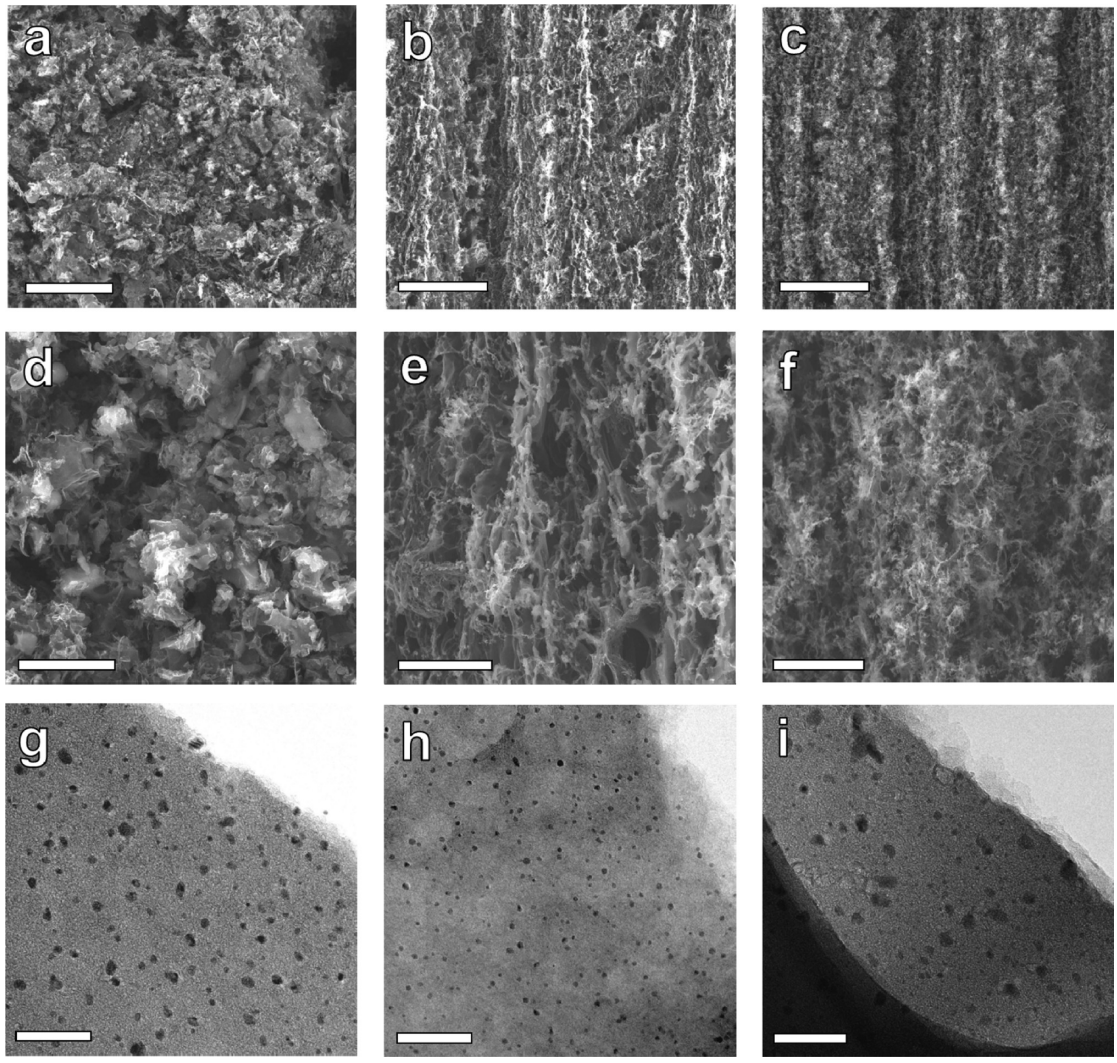

Figure 1. Morphology of MO-LIG. Lower magnification SEM images of (a) 5Co-LIG, (b) 5Mo-LIG, and (c) 5Fe-LIG. The scale bars are 50 μm. Higher magnification SEM images of (d) 5Co-LIG, (e) 5Mo-LIG, and (f) 5Fe-LIG. The scale bars are 10 μm. TEM images of (g) 5Co-LIG, (h) 5Mo-LIG, and (i) 5Fe-LIG. The scale bars are 100 nm.

to a slight decrease of BET surface areas (Table S1), whereas no significant deviation in nanocrystal size distribution was observed after the annealing process, as evidenced by the TEM images of the corresponding MO-LIG-A (Figure S2d−i). The size distribution of MoO_2 nanoparticles was smaller than those of Co_3O_4 or Fe_3O_4, possibly because of the higher dispersibility and solubility of that metal complex in the precursor mixed solvent and consequently lower tendency to agglomerate. The nanocrystals in MO-LIGs display clear lattice fringes in the high-resolution TEM (Figure 2). As shown in Figure 2a and b, the Co_3O_4 crystal phase planar spacing of the (311) and (400) planes are 0.24 and 0.20 nm, respectively. Similarly, planar spacings of 0.33 and 0.24 nm for the (110) and (111) planes of MoO_2 (Figure 2c,d) and 0.24 and 0.29 nm for the (022) and (112) planes of Fe_3O_4 (Figure 2e,f) were also observed.

The structures of MO-LIGs were further revealed by Raman and X-ray diffraction (XRD). As shown in the Raman spectra (Figure 3a−c), the peaks at ∼1585 and 2700 cm^{-1} correspond to the G and 2D peaks of graphene. The I_G/I_{2D} ratios vary from 2 to 3 across all the samples, indicating that the graphene is few-layered.[2,27] A decrease in D peak (1353 cm^{-1}) is observed after annealing, suggesting a lower degree of defects in MO-LIG-A. The XRD spectra of MO-LIG (Figure 3d−f) further confirm the graphitic structure of LIG. The typical (002) peaks of graphene at ∼26° reveal that the d_{002} spacings are ∼0.34 nm. The crystalline size along the *c* axis, L_c, and the domain size along the *a* axis, L_a, for 5Co-LIG, 5Mo-LIG, and 5Fe-LIG were calculated from the full width at half-maximum of the (002) and (100) peaks. L_c and L_a are 4.9 and 11.6 nm; 4.0 and 8.3 nm; and 2.7 and 10.4 nm, respectively (Supporting Equations). After annealing at 750 °C under argon, the (002) and (100) peaks became significantly sharper, suggesting a larger crystalline domain along the *a* and *c* axes. The crystal structures of metal oxide nanocrystals are also present in Figure 3d−f,

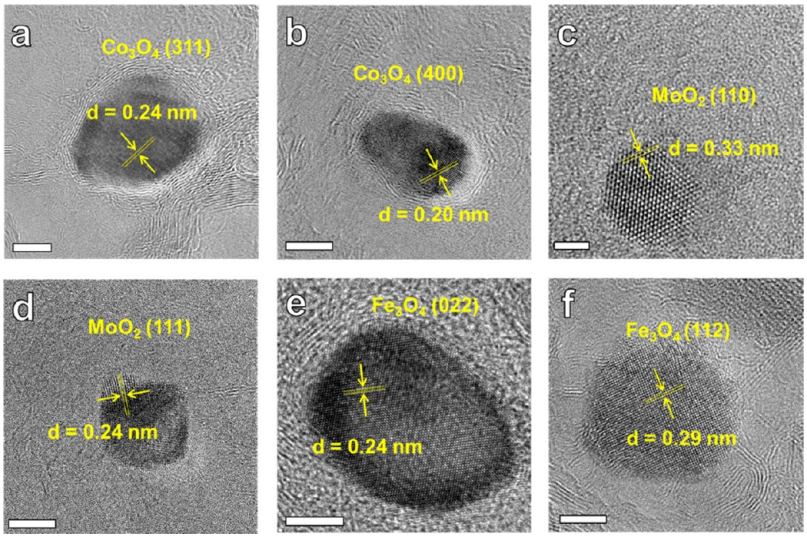

Figure 2. High-resolution TEM images showing crystalline metal oxide in LIG. (a, b) Co_3O_4 in 5Co-LIG, (c, d) MoO_2 in 5Mo-LIG, and (e, f) Fe_3O_4 in 5Fe-LIG. The scale bar in (a) is 2 nm, and the scale bars in (b)−(f) are 5 nm.

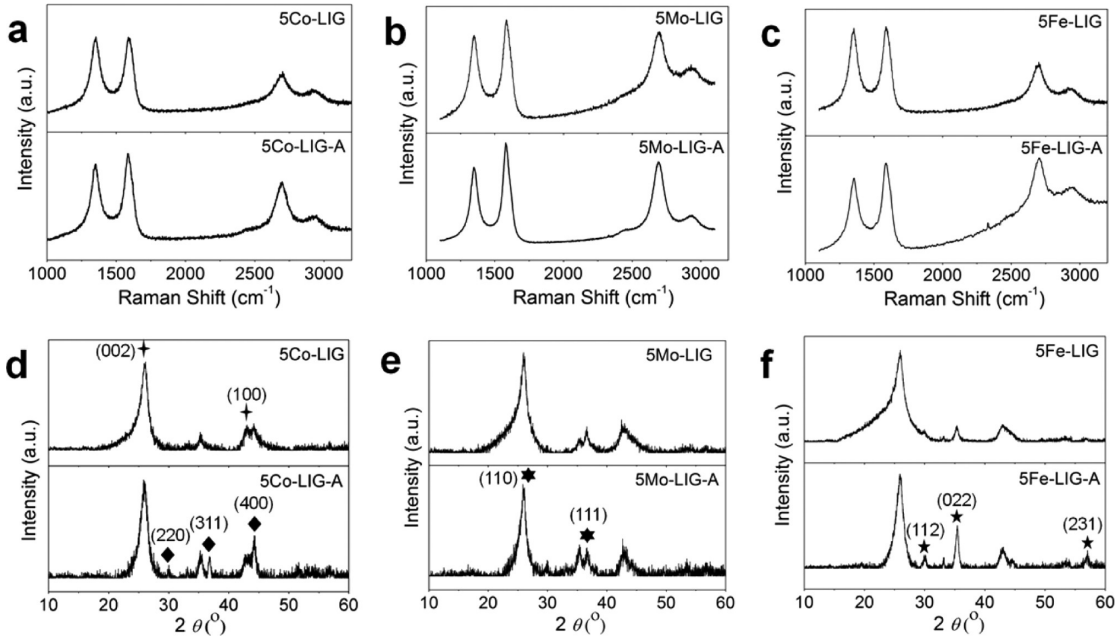

Figure 3. Structure characterizations of MO-LIG and MO-LIG-A. Raman spectra of (a) cobalt-, (b) molybdenum-, and (c) iron-containing LIG before and after annealing. XRD spectra of (d) cobalt (PDF #98-000-0166)-, (e) molybdenum (PDF #04-005-4546)-, and (f) iron (PDF #04-007-2412)-containing LIG before and after annealing.

yet the intensities are much weaker compared to those of graphene due to the low concentration of the materials. The annealing process does not lead to a significant shift in 2θ of nanocrystals, yet the corresponding XRD peaks became more intense, suggesting that the nanocrystals maintained the same crystal phases yet with more crystalline structures after annealing. The planar spacings of the lattice planes calculated from the XRD spectra were consistent with those from direct measurement of high-resolution TEM images (Supporting equations).

The chemical composition of the MO-LIGs was analyzed by X-ray photoelectron spectroscopy (XPS). As shown in Figure S3, the high-resolution C 1s XPS spectrum primarily consisted of a peak centered at 284.5 eV, indicating that the carbons are mainly C−C bonded; the N 1s peak location at ~400 eV indicates that the nitrogen atoms are mainly in pyrrolic structures. As to the metals, the presence of the major peak at 780 eV and satellite peak at 785 eV in the Co 2p XPS spectrum (Figure S3d) reveal that the cobalt contains both +2 and +3 oxidation states.[28] Similarly, molybdenum is in oxidation states of +2 and +6, and iron is in oxidation states of +2 and +3. No apparent shift occurs in the C 1s, O 1s, Co 2p, Mo 3d, and Fe 2p XPS spectra after annealing, which suggests the environments

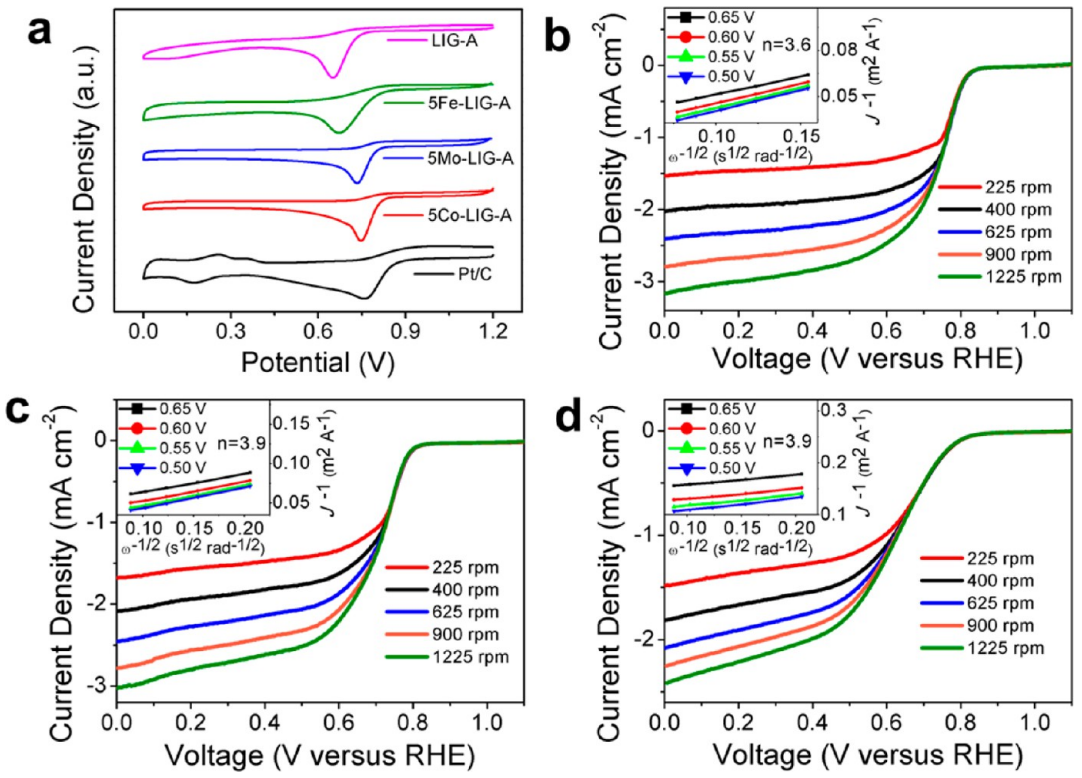

Figure 4. Oxygen reduction catalytic performance of MO-LIG-A. (a) Cyclic voltammetry curves of LIG-A, 5Co-LIG-A, 5Fe-LIG-A, 5Mo-LIG-A, and Pt/C in O_2-saturated 0.1 M KOH at a scan rate of 5 mV s^{-1}. Rotating-disk voltammograms of (b) 5Co-LIG-A, (c) 5Mo-LIG-A, and (d) 5Fe-LIG-A in O_2-saturated 0.1 M KOH at a scan rate of 5 mV s^{-1} at different rotating speeds. The sample loadings are ~0.08 mg cm^{-2}. Insets are the corresponding Koutecky–Levich plot at different potentials.

of these elements remain unchanged. However, the N 1s peak shifts from 400 to 401 eV after annealing, indicating a transformation of pyrrolic nitrogen into quaternary nitrogen.[29] A shoulder peak corresponding to the pyridinic nitrogen at 398.5 eV also becomes more significant after annealing. The atomic concentrations of the elements in MO-LIG and MO-LIG-A are summarized in Table S2. All the samples contain >90 at. % carbon and <1 at. % metal.

Electrocatalysis Performance. Although the atomic concentrations of metal elements are low, MO-LIG-A exhibits effective and efficient electrocatalytic activity in converting O_2 into OH^-. Figure 4a displays the cyclic voltammetry (CV) curves of MO-LIG-A and commercial Pt/C loaded on glassy carbon in an O_2-saturated 0.1 M KOH aqueous solution. The $E_{1/2}$ redox peaks of O_2/OH^- of 5Co-LIG-A, 5Fe-LIG-A, and 5Mo-LIG-A are 0.79 V, 0.74, and 0.77 V, respectively. These values are comparable to that of Pt/C at 0.81 V. The ORR kinetics of the MO-LIG-A were further assessed by linear swept voltammetry (LSV) using a rotating-disk electrode (RDE) in 0.1 M KOH solution (Figure 4b–d). Linear fitting of the corresponding Koutecky–Levich plots at the selected potentials (insets in Figure 4b–d; Supporting equations) reveals that the electron transfer numbers (n) are 3.6, 3.9, and 3.9 for 5Co-LIG-A, 5Mo-LIG-A, and 5Fe-LIG-A, respectively, which are close to a full reduction ($n = 4$) of O_2 to OH^-.[30,31] However, the ORR catalytic efficiency is much inferior for annealed LIG without metal oxide nanocrystals (LIG-A). As shown in Figure 4, the $E_{1/2}$ redox peak of LIG-A is at ~0.66 V, which is much lower than that of MO-LIG-A. The electron transfer number of LIG-A derived from the Koutecky–Levich plot (Figure S4a) also drops to 2.7, indicating a more favorable 2e reduction of O_2 toward HO_2^-. The samples without annealing also present lower catalytic activity, as evidenced in Figure S4b–d, where the electron transfer numbers are 2.6, 3.1, and 2.3 for 5Co-LIG, 5Mo-LIG, and 5Fe-LIG, respectively. The enhanced catalytic performance after the annealing process is thought to be due to the increased crystalline structure and the improved contact between metal oxide nanocrystals and graphene,[32] producing a strong synergistic interaction.[12,13,33]

The ORR electrocatalytic activity of MO-LIG-A was further analyzed using Tafel slopes (Figure 5a) derived from the mass-transport correction of the LSV curves in RDE (Supporting equations). The calculated Tafel slopes for 5Co-LIG-A and 5 Mo-LIG-A are 50 and 57 mV $decade^{-1}$, respectively. However, 5Fe-LIG-A has a Tafel slope of 102 mV $decade^{-1}$, suggesting a lower ORR activity. These values are comparable to graphene-based composites in the literature. For example, a value of 42 mV $decade^{-1}$ for the Co_3O_4/N-rmGO,[12] ~110 mV $decade^{-1}$ for Fe-N-rGO,[34] and ~200 mV $decade^{-1}$ for MoOx/GCE[35] are reported. The high catalytic

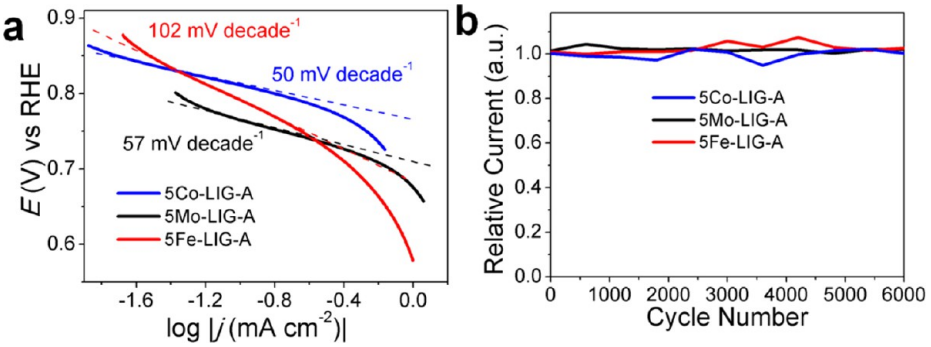

Figure 5. Stability and activity of MO-LIG-A as oxygen reduction catalysts. (a) Tafel plots of 5Co-LIG-A, 5Mo-LIG-A, and 5Fe-LIG-A derived by mass-transport correction of corresponding RDE data. (b) Relative current of 5Co-LIG-A, 5Mo-LIG-A, and 5Fe-LIG-A collected at 0.4 V for 6000 cycles in 0.1 M KOH at a scan rate of 100 mV s^{-1}.

activity of MO-LIG-A is impressive since the metal loading in the materials was <1 at. %, concentrations that are much smaller than reported in other studies.[12,13,31,34,36] Remarkably, these MO-LIG-As also exhibit extraordinary ORR catalytic stability. As shown in Figure 5b, the current densities of MO-LIG-As at 0.4 V remain mostly unchanged after 6000 cycles in 0.1 M KOH solution. The stability in the presence of methanol was also examined. As shown in Figure S5, no significant drops in current were observed after the addition of methanol, indicating the MO-LIG-A materials are not heavily susceptible to the poisoning effect of methanol.

Besides functioning as ORR electrocatalyst, the tunable nature of nanoparticles in LIG through lateral doping makes it possible to modify the material for uses in other electrocatalytic reactions. For example, reaction of 5Mo-LIG with sulfur at 350 °C leads to the conversion of MoO_2 to MoS_2 nanocrystals (MoS_2-LIG). The successful conversion was confirmed using TEM analysis (Figure S6), where a d_{100} = 0.32 nm was observed.[37] High-resolution XPS of Mo 3d and S 2p (Figure S7) also further verified the identity of MoS_2. As shown in Figure S7a, after reaction with sulfur, the major peak (Mo $3d_{5/2}$) shifts from 232.3 to 228.9 eV, where $Mo^{4+}3d_{5/2}$ is located. The HER performance was assessed by LSV of MoS_2-LIG in 0.5 M H_2SO_4 with an onset overpotential of ~200 mV and a Tafel slope of 97 mV $decade^{-1}$ (Figure S8). The low current observed (~2 mA cm^{-2} at 100 mV off onset potential) is attributed to the low concentration of MoS_2 nanocrystals, which is only HER active at the edge.[38,39] Electrochemical surface area (ECSA) measurement (Figure S9; Supporting Equations) revealed that A_{ECSA} = 24 cm^2, which also confirms the low concentration and small active area.

CONCLUSION

In summary, we have developed a cost-effective method for preparation of nanocrystals embedded in graphene. With a metal loading of less than 1 at. %, these materials exhibit excellent ORR catalytic activity, which primarily comes from the metal oxide nanocrystals. The performance of the MO-LIG is tunable by varying the metal complex precursor or doping with other elements. This may make it possible to use the MO-LIGs and their derivatives in various applications.

METHODS

Materials Synthesis. Poly(pyromellitic dianhydride-*co*-4,4′-oxidianiline amic acid) (7.8 g) solution (12.8 wt % in *N*-methyl-2-pyrrolidone/aromatic solvent, 80:20, 25038-81-7, Sigma-Aldrich) was used as a precursor solution for formation of a polyimide sheet. Cobalt(III) acetylacetonate (1 mL of 50 mg/mL in NMP, 21679-46-9, Sigma-Aldrich), iron(III) acetylacetonate (1 mL of 50 mg/mL in NMP, 14024-18-1, Sigma-Aldrich), or molybdenyl(VI) acetylacetonate (1 mL of 50 mg/mL in NMP, 17524-05-9, Sigma-Aldrich) was added to the PAA solution with bath sonication (Cole Parmer, model 08849-00) until a homogeneous mixture formed. The solution was poured into an aluminum dish (~5 cm in diameter and ~1 cm in depth), and the dish was placed in a vacuum oven at 60 °C under ~120 mmHg vacuum for 3 d to evaporate the solvent. The film-forming process was completed using a hydraulic press (Carver, no. 3912) with an applied load of 3×10^5 Pa at 200 °C for 30 min to dehydrate and form the metal-complex-containing PI sheet. Laser induction was then conducted on the metal-complex-containing PI substrate with a 10.6 μm carbon dioxide (CO_2) laser cutter system (Universal X-660 laser cutter platform with a pulse duration of ~14 μs). The laser power was fixed at 4.8 W during laser induction. All experiments were performed under ambient conditions. The annealing process was performed in a CVD furnace. Typically, MO-LIG powder was heated at 750 °C in a standard one-inch quartz tube furnace for 30 min. The pressure inside the quartz tube was ~100 mTorr with continuous Ar flow (50 sccm).

Characterization. SEM was performed using an FEI Quanta 400 high-resolution field emission scanning electron microscope in high-vacuum mode. The BET surface area was measured using a Quantachrome Autosorb-3B surface analyzer, and the sample was dried at 110 °C under vacuum for 16 h before the experiment. TEM was performed using a JEOL 2100 field emission gun transmission electron microscope. XPS spectra were taken on a PHI Quantera SXM scanning X-ray microprobe with a base pressure of 5×10^{-9} Torr. A pass energy of 26 eV with a 200 μm beam size was used for elemental spectra. Raman spectroscopy (Renishaw inVia) was performed at 514.5 nm laser excitation at a power of ~10 mW. XRD was conducted on a Rigaku D/Max Ultima II with Cu Kα radiation. All of the samples for SEM, TEM, XPS, Raman, BET, and XRD were powder that was scratched from the LIG films.

Electrochemical Characterization. CV and RDE studies of ORR were conducted in a home-built electrochemical cell using a mercury/mercury oxide electrode (CHI 152, CH Instruments) as the reference electrode and a Pt wire as the counter electrode. The currents were collected using a CHI 608D workstation (CH Instruments). For the preparation of electrode for the ORR test, 2 mg of catalyst was dispersed in 2 mL of 0.5 wt % Nafion aqueous solution by sonication (Cole Parmer, model 08849-00) until a homogeneous ink was formed. Then, 16 μL of the catalyst ink was loaded onto a glassy carbon electrode (5 mm in diameter, Pine Instrument) and dried slowly in air. A flow of O_2 was maintained in the electrolyte during the measurement to ensure continuous O_2 saturation. A saturated calomel electrode (CHI 150, CH Instruments) was used in the HER measurement. For preparation of the electrode for the HER test, 4 mg of catalyst was dispersed in 1 mL of 0.5 wt % Nafion aqueous solution by sonication until a homogeneous ink was formed. Then, 5 μL of the catalyst ink was loaded onto a glassy carbon electrode (CHI 104, CH Instruments) and dried slowly in air. Measurements were conducted in 0.5 M H_2SO_4 at a scan rate of 5 mV s^{-1}. All the reference electrodes were calibrated with respect to the reversible hydrogen electrode. The calibrations were conducted in high-purity hydrogen-saturated electrolyte with a Pt wire as the working electrode at a scan rate of 1 mV s^{-1}. The average of the two potentials of each CV curve where the current crossed zero was taken to be the thermodynamic potential. For the mercury/mercury oxide electrode, E(RHE) = E(Hg/HgO) + 0.901 V in 0.1 M KOH. For the saturated calomel electrode, E(RHE) = E(SCE) + 0.260 V in 0.5 M H_2SO_4.

Conflict of Interest: The authors declare no competing financial interest.

Acknowledgment. This work was supported by the Air Force Office of Scientific Research (FA9550-14-1-0111) and the Air Force Office of Scientific Research MURI (FA9550-12-1-0035). J.L. acknowledges the financial support from MU start-up fund, University of Missouri Research Board (DN304), and Oak Ridge Associated Universities (ORAU) Ralph E. Powe Junior Faculty Award. R.Y. and Z.P. designed the experiments, carried out the reactions, and studied the electrocatalysis. T.W. and J.Z. assisted the sample preparation and electrocatalysis. Y.X. performed the TEM analysis. Y.L. performed additional experiments. L.G.N. drew the scheme. J.L. contributed to the experimental design. J.M.T. oversaw all phases of the research and corrected the manuscript.

Supporting Information Available: The Supporting Information is available free of charge on the ACS Publications website at DOI: 10.1021/acsnano.5b04138.

Additional methods, figures, and data (PDF)

REFERENCES AND NOTES

1. Wang, X.; Zhang, Y.; Zhi, C.; Wang, X.; Tang, D.; Xu, Y.; Weng, Q.; Jiang, X.; Mitome, M.; Golberg, D.; et al. Three-Dimensional Strutted Graphene Grown by Substrate-Free Sugar Blowing for High-Power-Density Supercapacitors. *Nat. Commun.* **2013**, *4*, 2905.
2. Lin, J.; Peng, Z. W.; Liu, Y. Y.; Ruiz-Zepeda, F.; Ye, R. Q.; Samuel, E. L. G.; Yacaman, M. J.; Yakobson, B. I.; Tour, J. M. Laser-Induced Porous Graphene Films from Commercial Polymers. *Nat. Commun.* **2014**, *5*, 5714.
3. Schwierz, F. Graphene Transistors: Status, Prospects, and Problems. *Proc. IEEE* **2013**, *101*, 1567–1584.
4. Pang, S.; Hernandez, Y.; Feng, X.; Mullen, K. Graphene as Transparent Electrode Material for Organic Electronics. *Adv. Mater.* **2011**, *23*, 2779–2795.
5. Liu, Y.; Wu, X.; Zhao, Y.; Zeng, X. C.; Yang, J. Half-Metallicity in Hybrid Graphene/Boron Nitride Nanoribbons with Dihydrogenated Edges. *J. Phys. Chem. C* **2011**, *115*, 9442–9450.
6. Jeon, I. Y.; Zhang, S.; Zhang, L. P.; Choi, H. J.; Seo, J. M.; Xia, Z. H.; Dai, L. M.; Baek, J. B. Edge-Selectively Sulfurized Graphene Nanoplatelets as Efficient Metal-Free Electrocatalysts for Oxygen Reduction Reaction: The Electron Spin Effect. *Adv. Mater.* **2013**, *25*, 6138–6145.
7. Chen, G.; Liu, Y.; Liu, F.; Zhang, X. Fabrication of Three-Dimensional Graphene Foam with High Electrical Conductivity and Large Adsorption Capability. *Appl. Surf. Sci.* **2014**, *311*, 808–815.
8. Bolotin, K. I.; Sikes, K. J.; Jiang, Z.; Klima, M.; Fudenberg, G.; Hone, J.; Kim, P.; Stormer, H. L. Ultrahigh Electron Mobility in Suspended Graphene. *Solid State Commun.* **2008**, *146*, 351–355.
9. Wu, Z. S.; Ren, W.; Gao, L.; Zhao, J.; Chen, Z.; Liu, B.; Tang, D.; Yu, B.; Jiang, C.; Cheng, H. M. Synthesis of Graphene Sheets with High Electrical Conductivity and Good Thermal Stability by Hydrogen Arc Discharge Exfoliation. *ACS Nano* **2009**, *3*, 411–417.
10. Lee, C.; Wei, X.; Kysar, J. W.; Hone, J. Measurement of the Elastic Properties and Intrinsic Strength of Monolayer Graphene. *Science* **2008**, *321*, 385–388.
11. Xia, J.; Chen, F.; Li, J.; Tao, N. Measurement of the Quantum Capacitance of Graphene. *Nat. Nanotechnol.* **2009**, *4*, 505–509.
12. Liang, Y.; Li, Y.; Wang, H.; Zhou, J.; Wang, J.; Regier, T.; Dai, H. Co_3O_4 Nanocrystals on Graphene as a Synergistic Catalyst for Oxygen Reduction Reaction. *Nat. Mater.* **2011**, *10*, 780–786.
13. Devadoss, A.; Sudhagar, P.; Das, S.; Lee, S. Y.; Terashima, C.; Nakata, K.; Fujishima, A.; Choi, W. B.; Kang, Y. S.; Paik, U. Synergistic Metal-Metal Oxide Nanoparticles Supported Electrocatalytic Graphene for Improved Photoelectrochemical Glucose Oxidation. *ACS Appl. Mater. Interfaces* **2014**, *6*, 4864–4871.
14. Dalfovo, M. C.; Lacconi, G. I.; Moreno, M.; Yappert, M. C.; Sumanasekera, G. U.; Salvarezza, R. C.; Ibanez, F. J. Synergy between Graphene and Au Nanoparticles (Heterojunction) Towards Quenching, Improving Raman Signal, and UV Light Sensing. *ACS Appl. Mater. Interfaces* **2014**, *6*, 6384–6391.
15. Beliatis, M. J.; Gandhi, K. K.; Rozanski, L. J.; Rhodes, R.; McCafferty, L.; Alenezi, M. R.; Alshammari, A. S.; Mills, C. A.; Jayawardena, K. D. G. I.; Henley, S. J.; et al. Hybrid Graphene-Metal Oxide Solution Processed Electron Transport Layers for Large Area High-Performance Organic Photovoltaics. *Adv. Mater.* **2014**, *26*, 2078–2083.
16. Shang, L.; Bian, T.; Zhang, B. H.; Zhang, D. H.; Wu, L. Z.; Tung, C. H.; Yin, Y. D.; Zhang, T. R. Graphene-Supported Ultrafine Metal Nanoparticles Encapsulated by Mesoporous Silica: Robust Catalysts for Oxidation and Reduction Reactions. *Angew. Chem., Int. Ed.* **2014**, *53*, 250–254.
17. Shin, S. I.; Go, A.; Kim, I. Y.; Lee, J.; Lee, Y.; Hwang, S. J. A Beneficial Role of Exfoliated Layered Metal Oxide Nanosheets in Optimizing the Electrocatalytic Activity and Pore Structure of Pt-Reduced Graphene Oxide Nanocomposites. *Energy Environ. Sci.* **2013**, *6*, 608–617.
18. Kundu, P.; Nethravathi, C.; Deshpande, P. A.; Rajamathi, M.; Madras, G.; Ravishankar, N. Ultrafast Microwave-Assisted Route to Surfactant-Free Ultrafine Pt Nanoparticles on Graphene: Synergistic Co-Reduction Mechanism and High Catalytic Activity. *Chem. Mater.* **2011**, *23*, 2772–2780.
19. Qiu, B. C.; Xing, M. Y.; Zhang, J. L. Mesoporous TiO_2 Nanocrystals Grown *in Situ* on Graphene Aerogels for High Photocatalysis and Lithium-Ion Batteries. *J. Am. Chem. Soc.* **2014**, *136*, 5852–5855.
20. Qiu, B. C.; Xing, M. Y.; Zhang, J. L. Stober-Like Method to Synthesize Ultralight, Porous, Stretchable Fe_2O_3/Graphene Aerogels for Excellent Performance in Photo-Fenton Reaction and Electrochemical Capacitors. *J. Mater. Chem. A* **2015**, *3*, 12820–12827.
21. El-Kady, M. F.; Strong, V.; Dubin, S.; Kaner, R. B. Laser Scribing of High-Performance and Flexible Graphene-Based Electrochemical Capacitors. *Science* **2012**, *335*, 1326–1330.
22. Peng, Z.; Ye, R.; Lin, J.; Samuel, E. L. G.; Tour, J. M. Flexible and Stackable Laser-Induced Graphene Supercapacitors. *ACS Appl. Mater. Interfaces* **2015**, *7*, 3414–3419.
23. Peng, Z.; Ye, R.; Mann, J. A.; Zakhidov, D.; Li, Y.; Smalley, P. R.; Lin, J.; Tour, J. M. Flexible Boron-Doped Laser-Induced Graphene Microsupercapacitors. *ACS Nano* **2015**, *9*, 5868–5875.

24. Paek, S. M.; Yoo, E.; Honma, I. Enhanced Cyclic Performance and Lithium Storage Capacity of SnO_2/Graphene Nanoporous Electrodes with Three-Dimensionally Delaminated Flexible Structure. *Nano Lett.* **2009**, *9*, 72–75.
25. Wang, X. Y.; Zhou, X. F.; Yao, K.; Zhang, J. G.; Liu, Z. P. A SnO_2/Graphene Composite as a High Stability Electrode for Lithium Ion Batteries. *Carbon* **2011**, *49*, 133–139.
26. Liu, H. D.; Huang, J. M.; Xiang, C. J.; Liu, J.; Li, X. L. *In Situ* Synthesis of SnO_2 Nanosheet/Graphene Composite as Anode Materials for Lithium-Ion Batteries. *J. Mater. Sci.: Mater. Electron.* **2013**, *24*, 3640–3645.
27. Sun, Z.; Raji, A. R. O.; Zhu, Y.; Xiang, C. S.; Yan, Z.; Kittrell, C.; Samuel, E. L. G.; Tour, J. M. Large-Area Bernal-Stacked Bi-, Tr-, and Tetralayer Graphene. *ACS Nano* **2012**, *6*, 9790–9796.
28. Tan, B. J.; Klabunde, K. J.; Sherwood, P. M. A. XPS Studies of Solvated Metal Atom Dispersed Catalysts - Evidence for Layered Cobalt Manganese Particles on Alumina and Silica. *J. Am. Chem. Soc.* **1991**, *113*, 855–861.
29. Kumar, B.; Asadi, M.; Pisasale, D.; Sinha-Ray, S.; Rosen, B. A.; Haasch, R.; Abiade, J.; Yarin, A. L.; Salehi-Khojin, A. Renewable and Metal-Free Carbon Nanofibre Catalysts for Carbon Dioxide Reduction. *Nat. Commun.* **2013**, *4*, 2849.
30. Yang, S.; Feng, X.; Wang, X.; Mullen, K. Graphene-Based Carbon Nitride Nanosheets as Efficient Metal-Free Electrocatalysts for Oxygen Reduction Reactions. *Angew. Chem., Int. Ed.* **2011**, *50*, 5339–5343.
31. Mayrhofer, K. J. J.; Strmcnik, D.; Blizanac, B. B.; Stamenkovic, V.; Arenz, M.; Markovic, N. M. Measurement of Oxygen Reduction Activities *via* the Rotating Disc Electrode Method: From Pt Model Surfaces to Carbon-Supported High Surface Area Catalysts. *Electrochim. Acta* **2008**, *53*, 3181–3188.
32. Leong, W. S.; Nai, C. T.; Thong, J. T. L. What Does Annealing Do to Metal-Graphene Contacts? *Nano Lett.* **2014**, *14*, 3840–3847.
33. He, S.; Yu, Y.; Chen, Z.; Shi, Q.; Zhang, L. Synergistic Effect of Graphene and Multiwalled Carbon Nanotubes on a Glassy Carbon Electrode for Simultaneous Determination of Uric Acid and Dopamine in the Presence of Ascorbic Acid. *Anal. Lett.* **2015**, *48*, 248–258.
34. Byon, H. R.; Suntivich, J.; Shao-Horn, Y. Graphene-Based Non-Noble-Metal Catalysts for Oxygen Reduction Reaction in Acid. *Chem. Mater.* **2011**, *23*, 3421–3428.
35. Yavuz, E.; Ozdokur, K. V.; Cakar, I.; Kocak, S.; Ertas, F. N. Electrochemical Preparation, Characterization of Molybdenum-Oxide/Platinum Binary Catalysts and Its Application to Oxygen Reduction Reaction in Weakly Acidic Medium. *Electrochim. Acta* **2015**, *151*, 72–80.
36. Mao, S.; Wen, Z.; Huang, T.; Hou, Y.; Chen, J. High-Performance Bi-Functional Electrocatalysts of 3D Crumpled Graphene-Cobalt Oxide Nanohybrids for Oxygen Reduction and Evolution Reactions. *Energy Environ. Sci.* **2014**, *7*, 609–616.
37. Yu, Y.; Li, C.; Liu, Y.; Su, L.; Zhang, Y.; Cao, L. Controlled Scalable Synthesis of Uniform, High-Quality Monolayer and Few-Layer MoS_2 Films. *Sci. Rep.* **2013**, *3*, 1866.
38. Kibsgaard, J.; Jaramillo, T. F.; Besenbacher, F. Building an Appropriate Active-Site Motif into a Hydrogen-Evolution Catalyst with Thiomolybdate $[Mo_3S_{13}]^{(2-)}$ Clusters. *Nat. Chem.* **2014**, *6*, 248–253.
39. Hinnemann, B.; Moses, P. G.; Bonde, J.; Jorgensen, K. P.; Nielsen, J. H.; Horch, S.; Chorkendorff, I.; Norskov, J. K. Biomimetic Hydrogen Evolution: MoS_2 Nanoparticles as Catalyst for Hydrogen Evolution. *J. Am. Chem. Soc.* **2005**, *127*, 5308–5309.